Electric Power Systems Research 254 (2026) 112625

Contents lists available at ScienceDirect

Electric Power Systems Research

journal homepage: www.elsevier.com/locate/epsr

IAHO: Integrated Andronov-Hopf oscillator for providing ancillary services with single-phase grid-forming inverters

Hamed Rezazadeh [a], Mohammad Monfared [a,*], Meghdad Fazeli [a], Saeed Golestan [b]

[a] Department of Electronic and Electrical Engineering, Swansea University, SA1 8EN Swansea, UK
[b] AAU Energy, Aalborg University, 9220 Aalborg East, Denmark

ARTICLE INFO

Keywords:
Battery energy storage system (BESS)
Grid-forming (GFM) inverters
Transient stability
Virtual inertia
Virtual oscillator control (VOC)

ABSTRACT

The increasing deployment of renewable energy sources is reducing system inertia and challenging grid stability. Meanwhile, the growing penetration of grid-forming(GFM) inverters offers opportunities to enhance frequency and voltage support. Among GFM techniques, virtual oscillator control (VOC) has emerged as a promising approach due to its superior dynamic performance, yet existing VOC strategies exhibit limitations in inertia emulation, damping, and droop accuracy. This paper proposes a control strategy based on the integrated Andronov–Hopf oscillator (IAHO) that, for the first time, unifies virtual inertia, enhanced damping, and voltage-independent droop control into a single framework. A comprehensive small-signal analysis is conducted to design the damping controllers, while a large-signal analysis evaluates transient stability under severe grid disturbances. Theoretical insights are experimentally validated on a 2.5 kVA single-phase inverter. Results demonstrate that the proposed IAHO delivers a lower rate of change of frequency (RoCoF), higher frequency nadir, well-damped power dynamics, and enhanced active power support compared to conventional VOC-based strategies. Moreover, the IAHO ensures positive reactive power droop during voltage sags, providing superior transient stability.

1. Introduction

Modern power systems are undergoing a rapid transformation due to the growing penetration of renewable energy sources. Unlike conventional power plants, which inherently contribute to grid stability through the rotational inertia of synchronous generators, these renewable sources are typically interfaced through power electronic converters that do not provide inertial support by default. As a result, system inertia is declining, making the grid more susceptible to frequency instability and voltage deviations. To ensure reliable and resilient operation under these conditions, new grid-supportive resources are needed to provide essential ancillary services such as frequency regulation, voltage support, and operating reserves.

Battery energy storage systems (BESSs), such as electric vehicles and photovoltaic (PV) battery systems, are poised to play a key role in this context. However, to contribute effectively, their inverters must evolve from traditional grid-following control, which acts as a current source, to advanced grid-forming (GFM) control. GFM inverters function as voltage sources, enabling stand-alone operation and emulating the stabilising behaviour of synchronous generators. While research on GFM control has primarily focused on three-phase systems, the majority of residential BESS installations are single-phase, presenting unique challenges and opportunities for distributed grid support [1–3].

Among various GFM techniques, virtual oscillator control (VOC) has gained attention due to its time-domain implementation, based on instantaneous measurements, which avoids Phase-locked loop (PLL) structures and complex optimisation, and thus offers favourable dynamic performance with a relatively low computational burden [4]. VOC emulates the dynamic behaviour of nonlinear oscillators, such as dead-zone [5], Van der Pol [6], and Andronov–Hopf [7,8], with the latter being particularly suited for grid applications due to its harmonic-free voltage generation and dispatchable nature. However, despite its promise, existing Andronov–Hopf oscillator (AHO) strategies suffer from critical limitations that hinder their practical application. Early implementations like the unified VOC (uVOC) demonstrated basic GFM capability but lacked virtual inertia [9]. Subsequent efforts to

* Corresponding author.
E-mail addresses: 2251309@swansea.ac.uk (H. Rezazadeh), mohammad.monfared@swansea.ac.uk (M. Monfared), m.fazeli@swansea.ac.uk (M. Fazeli), sgd@energy.aau.dk (S. Golestan).

https://doi.org/10.1016/j.epsr.2025.112625
Received 6 October 2025; Received in revised form 11 December 2025; Accepted 12 December 2025
Available online 7 January 2026

integrate virtual inertia into the AHO dynamics (VI-AHO) inadvertently reduced the system's damping factor, leading to undesirable oscillatory behaviour [10,11]. To address this, a feedforward damping improvement strategy (Da-AHO) has been proposed, which improves damping while maintaining adequate virtual inertia [12]. However, all these approaches rely on a voltage-dependent droop coefficient in the active power loop (APL), which limits their ability to maintain consistent grid support during disturbances and leads to inaccuracies in power sharing. To overcome this, an enhanced AHO (EAHO) has been proposed in [13], where the APL droop is completely independent of the voltage. However, EAHO still lacks both virtual inertia and damping. Consequently, a unified AHO structure that simultaneously provides all necessary ancillary services is still lacking.

Furthermore, a critical gap exists in the analysis of transient stability. Most existing works focus on small-signal analysis around equilibrium points [8,14,15], which is inadequate when the system is subjected to large-signal disturbances, such as severe voltage sag [16]. While some recent studies have investigated the transient stability of AHO [17–20], they do not incorporate virtual inertia, which fundamentally modifies system dynamics and affects stability margins. Moreover, in all these studies, the APL droop coefficient varies with voltage, which introduces steady-state power-sharing errors. While a variety of damping and transient-stability enhancement techniques have been developed for virtual synchronous generators (VSGs) [21–24], comparable methods for VOC-based GFM inverters remain largely unexplored, despite the inherently superior dynamic response of VOCs compared to VSGs.

To address the limitations of existing AHO-based VOC strategies, this paper proposes an Integrated AHO (IAHO) control framework that unifies improved droop functionality, virtual inertia, and damping enhancement into a single and coordinated design. The key contributions of this work can be summarised as follows:

1) Development of the first unified AHO-based inverter control structure that simultaneously incorporates virtual inertia, damping enhancement, and a voltage-independent active power loop (APL) droop formulation.
2) Rigorous and holistic small-signal modelling and controller synthesis to analytically design and tune the integrated control blocks, followed by comparative evaluation against existing AHO variants.
3) Large-signal and transient stability assessment under severe disturbances to demonstrate robustness and performance superiority over conventional approaches.
4) Extensive experimental validations on a 2.5 kVA single-phase inverter platform, confirming that the proposed IAHO achieves voltage-independent active power droop coefficient, effective inertia emulation, and enhanced damping while improving transient stability performance.

The rest of this paper is organised as follows. Section II introduces the IAHO strategy and compares it with existing approaches. Section III presents the transient stability analysis, while Section IV validates the theoretical findings through experimental results. Finally, Section V concludes the paper.

2. Proposed IAHO

2.1. IAHO system configuration

Fig. 1 illustrates the proposed IAHO-based single-phase GFM inverter. In this configuration, L_f, R_f, and C_f denote the filter inductance, its parasitic resistance, and the filter capacitance, respectively. Z_L is the local load, and L_g and R_g represent the grid impedance. The DC link is represented by C_{dc} and V_{dc}, corresponding to the capacitance and voltage, respectively, and v_{pcc} denotes the voltage at the point of common coupling.

The AHO is a nonlinear time-domain controller implemented in the $\alpha\beta$ reference frame. According to Fig. 1, the control law governing the oscillator output voltage is given in (1):

$$\begin{bmatrix} \dot{v}_\alpha \\ \dot{v}_\beta \end{bmatrix} = \begin{bmatrix} \mu\left(V_{p0}^2 - V_p^2\right) & \omega_0' \\ \omega_0' & \mu\left(V_{p0}^2 - V_p^2\right) \end{bmatrix} \begin{bmatrix} v_\alpha \\ v_\beta \end{bmatrix} + \eta \frac{V_p^2}{2} \begin{bmatrix} 0 & -1 \\ 1 & 0 \end{bmatrix} \begin{bmatrix} y_\alpha' \\ y_\beta' \end{bmatrix} \tag{1}$$

where v_α and v_β are the oscillator output voltages in the $\alpha\beta$ reference frame, V_{p0} is the nominal voltage vector magnitude (V_p), and η and μ are

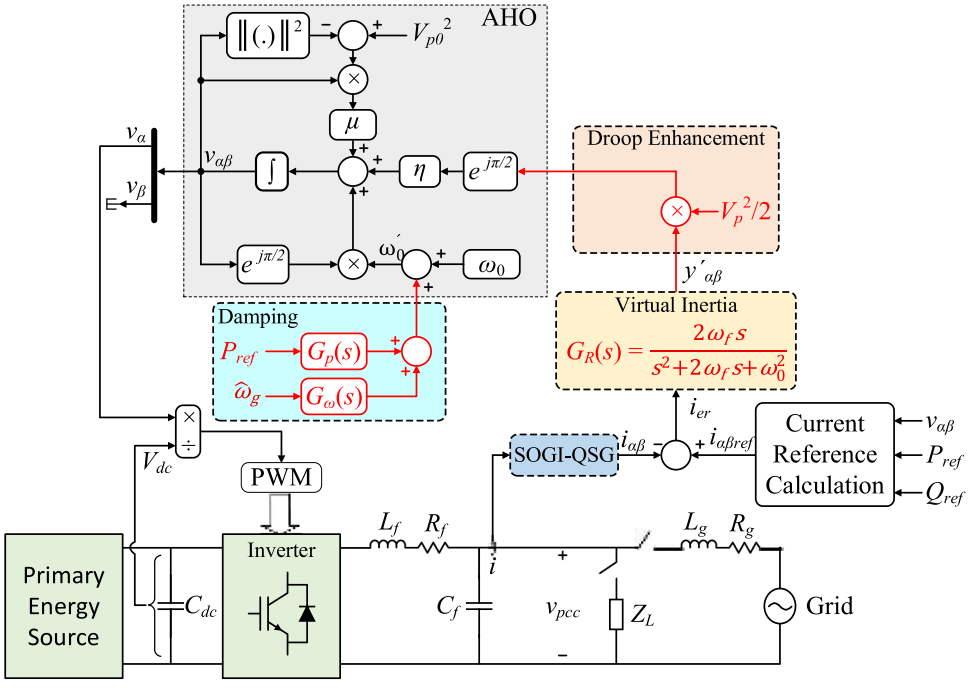

Fig. 1. Proposed IAHO-based single-phase GFM inverter.

the control parameters of AHO. In the proposed IAHO, virtual inertia is incorporated by means of a resonant controller acting on the current error (i_{er}) [11]. Thus, the output of the virtual inertia block, $y'_{\alpha\beta}$, is defined as:

$$y'_{\alpha\beta} = G_R(s)\left(i_{\alpha\beta ref} - i_{\alpha\beta}\right) \tag{2}$$

where $i_{\alpha\beta ref}$ is the inverter's reference current and $i_{\alpha\beta}$ is the measured inverter output current in the $\alpha\beta$ reference frame. Furthermore, $G_R(s)$ is the transfer function of the resonant controller shown in Fig. 1, where ω_f denotes its bandwidth and ω_0 is the nominal angular frequency. In single-phase systems, only the α-axis current is physically measurable. Therefore, i_β is usually generated using a second-order generalised integrator-based quadrature signal generator (SOGI-QSG), as shown in Fig. 2(a), with the corresponding equation in (3), where K_{so} is the SOGI-QSG gain [2].

$$\begin{cases} \dfrac{i_\alpha(s)}{i(s)} = \dfrac{K_{so}\omega\, s}{s^2 + K_{so}\omega\, s + \omega^2} \\ \dfrac{i_\beta(s)}{i(s)} = \dfrac{K_{so}\omega^2}{s^2 + K_{so}\omega\, s + \omega^2} \end{cases} \tag{3}$$

To improve damping, the IAHO employs two feedforward controllers that adapt the oscillator's centre frequency to deviations from its nominal value. This adjustment counteracts oscillations caused by changes in either the active power reference (P_{ref}) or the grid frequency (ω_g) [12]. The modified angular frequency, ω'_0, is defined as:

$$\omega'_0 = \omega_0 + G_p(s)P_{ref} + G_\omega(s)\,\widehat{\omega}_g \tag{4}$$

where $G_p(s)$ and $G_\omega(s)$ are feedforward controllers designed to mitigate oscillations induced by P_{ref} and ω_g, respectively. The estimated grid angular frequency, $\widehat{\omega}_g$, is obtained from a SOGI-based frequency-locked loop (SOGI-FLL), as illustrated in Fig. 2(b) [25]. The transfer function from the input frequency deviation ($\Delta\omega_g$) to the estimated frequency deviation ($\Delta\widehat{\omega}_g$) can be derived from the SOGI-FLL's small-signal model, as expressed in (5), and is used to tune its parameters in accordance with [25].

$$\begin{cases} G_{FLL}(s) = \dfrac{\Delta\widehat{\omega}_g(s)}{\Delta\omega_g(s)} = \dfrac{\omega^2_{n-FLL}}{s^2 + 2\xi_{FLL}\,\omega_{n-FLL}\,s + \omega^2_{n-FLL}} \\ K_{i-FLL} = 2\omega^2_{n-FLL},\ K_{p-FLL} = \dfrac{4\,\xi_{FLL}\,\omega_{n-FLL}}{\omega_0} \end{cases} \tag{5}$$

In the above equations, $K_{p\text{-}FLL}$ and $K_{i\text{-}FLL}$ are the proportional and integral gains of the SOGI-FLL, respectively, designed to achieve the desired damping factor (ζ_{FLL}) and natural frequency ($\omega_{n\text{-}FLL}$). In this paper, $\zeta_{FLL} = 0.9$ is selected to ensure adequate damping, and $\omega_{n\text{-}FLL} = 150$ rad/s is chosen as a compromise between bandwidth and noise immunity.

As demonstrated in [12], a low-pass filter (LPF) relationship exists between the average amplitudes of the SOGI-QSG input and output signals (denoted as $\bar{I}$ and $\bar{I}_{\alpha\beta}$). This relationship is expressed as:

$$\frac{\bar{I}_{\alpha\beta}(s)}{\bar{I}(s)} = \frac{K_{so}\omega/2}{s + K_{so}\omega/2} = \frac{1}{T_{so}s + 1} \tag{6}$$

where K_{so} is the SOGI-QSG gain and T_{so} is the LPF time constant. Furthermore [12], shows that the virtual inertia realisation by the resonant controller can also be approximated by an LPF:

$$\frac{\overline{Y'}(s)}{\overline{I_{er}}(s)} = \frac{\omega_f}{s + \omega_f} = \frac{1}{T_f s + 1} \tag{7}$$

where $\overline{Y'}$ and $\overline{I_{er}}$ are the averaged output and input amplitudes of the resonant controller, respectively. Here, ω_f is the resonant controller bandwidth, and $T_f = 1/\omega_f$.

Applying these LPF effects to (1) results in the dynamic equation given in (8). The detailed derivation of (6)-(8) is provided in Appendix A.

$$\begin{cases} \dot{V}_p = \mu\left(V_{p0}^2 - V_p^2\right)V_p + \eta V_p \dfrac{1}{T_f s + 1}\left(Q_{ref} - \dfrac{1}{T_{so}s + 1}Q\right) \\ \dot{\theta} = \omega = \omega'_0 + \eta\dfrac{1}{T_f s + 1}\left(P_{ref} - \dfrac{1}{T_{so}s + 1}P\right) \end{cases} \tag{8}$$

where Q_{ref} is the reactive power reference. Eq. (8) explicitly incorporates the effect of virtual inertia (via T_f) and damping (via ω'_0). In addition, the APL droop coefficient (η) becomes voltage-independent, thereby improving droop performance. In contrast, conventional controllers such as those presented in [9,11,12] exhibit a voltage-dependent droop coefficient of $2\eta/V_p{}^2$, which limits grid support capability and results in inaccurate power sharing.

2.2. Small-signal model

In this section, the small-signal model of the proposed IAHO is derived to facilitate the design of the feedforward damping transfer functions. Fig. 3 presents a simplified model of a single-phase inverter connected to the grid. Within the frequency range of interest, the delay due to digital control and PWM, and the effect of the filter capacitance can be neglected [9,12]. Accordingly, the switching-averaged model of the control output voltage v can be approximated as the inverter terminal voltage [9,12]. In this study, the grid impedance parameters are

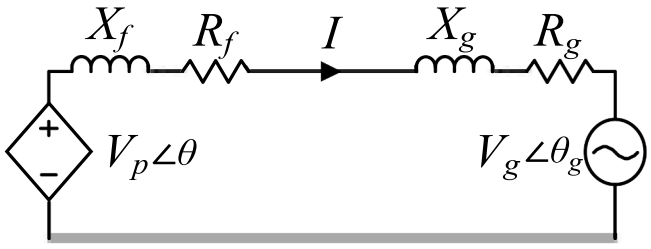

Fig. 3. Simplified model of a single-phase inverter connected to the grid.

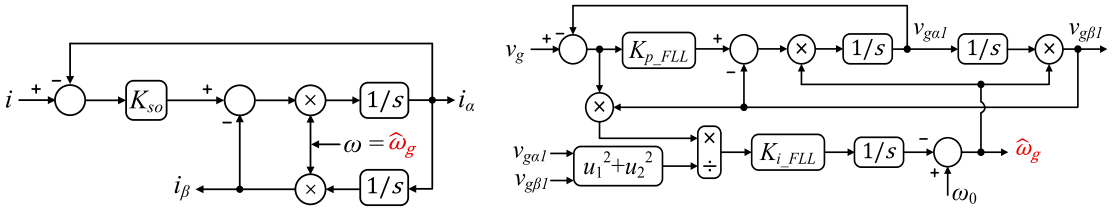

(a) (b)

Fig. 2. Block diagram of (a) SOGI-QSG [2] and (b) SOGI-FLL [25].

Table 1
Experimental parameters.

Parameters	Description	Value
P_0, Q_0	Rated active and reactive power	2000 W, 1500 var
V_{dc}	DC-link voltage	380 V
ω_0	Nominal angular frequency	$2\pi \times 50$ rad/s
V_{p0}	Nominal voltage amplitude	311 V
f_s	Switching frequency	20 kHz
L_f, R_f, C_f	Filter parameters	7 mH, 0.08 Ω, 3.9 μF
L_g, R_g	Grid parameters	1 mH, 1 Ω
μ, η	AHO control parameters	2.38×10^{-4}, 83.82
T_f	Virtual inertia control parameter	$1/(2\pi)$
K_{so}, ζ_{FLL}, $\omega_{n\text{-}FLL}$	SOGI and SOGI-FLL parameters	0.707, 0.9, 150 rad/s
ζ, ω_{n1}, ω_{n2}	AHO's dynamic parameters	0.85, 2π rad/s, 4π rad/s

selected as $L_g = 1$ mH and $R_g = 1\ \Omega$, yielding $R_g/X_g = 3.2$, which falls within the typical range for low- and medium-voltage networks [26]. Based on the experimental parameters listed in Table 1, the resistance-to-reactance ratio is calculated as $R_T/X_T = 0.39$, where $R_T = R_f + R_g$ and $X_T = \omega_0 (L_f + L_g)$. Accordingly, the active and reactive power exchanged between the inverter and the grid in Fig. 3 can be approximated as:

$$P \approx \frac{V_p\ V_g}{2X_T}\delta = K_s\delta,\ Q \approx \frac{V_p}{2X_T}(V_p - V_g) \tag{9}$$

where V_p and V_g denote the peak amplitudes of the inverter output and grid voltages, respectively, and δ=θ-θ_g is the phase angle difference between them.

Fig. 4 demonstrates the small-signal model of the proposed IAHO, derived from Eqs. (4), (8), and (9). In this model, $D = \eta$ represents the droop coefficient, K_s is defined in (9), and $G_{FLL}(s)$ is presented in (5).

Based on this model, the transfer functions of $\Delta P(s)/\Delta P_{ref}(s)$ and $\Delta P(s)/\Delta\omega_g(s)$ can be calculated by setting $\Delta\omega_g = 0$ and $\Delta P_{ref} = 0$, respectively:

$$\begin{cases} \dfrac{\Delta P(s)}{\Delta P_{ref}(s)} = \dfrac{D\ K_s + G_p(s)\ (T_f\ s+1)\ K_s}{T_{so}\ T_f\ s^3 + (T_f + T_{so})\ s^2 + s + D\ K_s} \\ \dfrac{\Delta P(s)}{\Delta\omega_g(s)} = \dfrac{(G_{FLL}(s)G_\omega(s) - 1)\ (T_f\ s+1)\ K_s}{T_{so}\ T_f\ s^3 + (T_f + T_{so})\ s^2 + s + D\ K_s} \end{cases} \tag{10}$$

Fig. 4 and Eq. (10) represent a unified small-signal model applicable to recent AHO-based control strategies. For uVOC [9] and EAHO [13], which do not incorporate virtual inertia or damping, the model and corresponding transfer functions are obtained by setting T_f=$G_p(s)$=$G_\omega(s)$=0, with $D = 2\eta/V_p^2$ for uVOC and $D = \eta$ for EAHO. For VI-AHO [11], the model is obtained by setting $G_p(s)$=$G_\omega(s)$=0 and $D = 2\eta/V_p^2$. The small-signal model of Da-AHO can be derived similarly by setting $D = 2\eta/V_p^2$ [12].

According to (10), proper tuning of the parameters enables independent shaping of the active power dynamics in response to both reference power and frequency disturbances. Unlike higher-order systems, a standard second-order system allows for intuitive tuning based on desired damping and natural frequency, as:

$$\begin{cases} \dfrac{\Delta P(s)}{\Delta P_{ref}(s)} = \dfrac{\omega_{n1}^2}{s^2 + 2\ \zeta\ \omega_{n1}\ s + \omega_{n1}^2} \\ \dfrac{\Delta P(s)}{\Delta\omega_g(s)} = -\dfrac{1}{D}\ \dfrac{\omega_{n2}^2}{s^2 + 2\ \zeta\ \omega_{n2}\ s + \omega_{n2}^2} \end{cases} \tag{11}$$

where ζ is the desired damping factor, and ω_{n1}, ω_{n2} are the desired natural frequencies for the active power response to $\Delta P_{ref}(s)$ and $\Delta\omega_g(s)$, respectively. The purpose of the damping-improvement strategy is to design the controllers $G_p(s)$ and $G_\omega(s)$ such that the third-order transfer functions in (10) are eventually simplified to the standard second-order forms in (11), which means the following set of equations should hold:

$$\begin{cases} \dfrac{D\ K_s + G_p(s)\ (T_f\ s+1)\ K_s}{T_{so}\ T_f\ s^3 + (T_f + T_{so})\ s^2 + s + D\ K_s} = \dfrac{\omega_{n1}^2}{s^2 + 2\ \zeta\ \omega_{n1}\ s + \omega_{n1}^2} \\ \dfrac{(G_{FLL}(s)G_\omega(s) - 1)\ (T_f\ s+1)\ K_s}{T_{so}\ T_f\ s^3 + (T_f + T_{so})\ s^2 + s + D\ K_s} = -\dfrac{1}{D}\ \dfrac{\omega_{n2}^2}{s^2 + 2\ \zeta\ \omega_{n2}\ s + \omega_{n2}^2} \end{cases} \tag{12}$$

By solving (12) for $G_p(s)$ and $G_\omega(s)$ and applying the simplifications described in [12], the feedforward controllers can be derived as:

$$\begin{cases} G_p(s) = \dfrac{b_1'\ s^2 + c_1 s}{d_1 s^3 + e_1 s^2 + f_1 s + g_1} \\ G_\omega(s) = \dfrac{a_2 s^3 + b_2 s^2 + c_2 s}{d_2 s^3 + e_2 s^2 + f_2 s + g_2} \end{cases} \tag{13}$$

The coefficients in (13) are given in (14), where $i = 1,2$.

$$\begin{cases} a_1 = \omega_{n1}^2 T_{so}\ T_f, b_1 = \omega_{n1}^2 (T_f + T_{so}) - DK_s, c_1 = \omega_{n1}^2 - DK_s 2\zeta\omega_{n1}, \\ b_1' = \dfrac{b_1 - \sqrt{b_1^2 - 4a_1 c_1}}{2}, a_2 = -\dfrac{\omega_{n2}^2 T_{so}\ T_f}{D} + K_s T_f, \\ b_2 = -\dfrac{\omega_{n2}^2 (T_f + T_{so})}{D} + K_s (1 + 2\zeta\omega_{n2} T_f), c_2 = -\dfrac{\omega_{n2}^2}{D} + K_s (T_f \omega_{n2}^2 + 2\zeta\omega_{n2}) \\ d_i = K_s T_f, e_i = K_s (1 + 2\zeta\omega_{ni} T_f), f_i = K_s (T_f \omega_{ni}^2 + 2\zeta\omega_{ni}), g_i = K_s \omega_{ni}^2 \end{cases} \tag{14}$$

2.3. Comparative analysis

In this section, the step responses of the proposed IAHO, derived from the transfer functions of the small-signal model, are compared against those of conventional approaches using the experimental parameters listed in Table 1. For all controllers, the AHO control parameters are designed to support the nominal active power (P_0) and reactive power (Q_0) under a 1 % grid frequency deviation ($\Delta f_{g,\max}$) and a 5 % change in voltage amplitude [9,12]. Furthermore, T_f is tuned to ensure that the maximum rate of change of frequency (RoCoF) remains below 3.5 Hz/s [12].

Fig. 5 presents the step response of $\Delta\omega(s)/\Delta P(s)$, $\Delta P(s)/\Delta P_{ref}(s)$, and $\Delta P(s)/\Delta\omega_g(s)$, obtained using MATLAB. Fig. 5(a) illustrates the inertial response in stand-alone mode, showing that VI-AHO, Da-AHO, and the proposed IAHO provide comparable inertial performance with low RoCoF, while the absence of virtual inertia is evident in the dynamics of uVOC and EAHO.

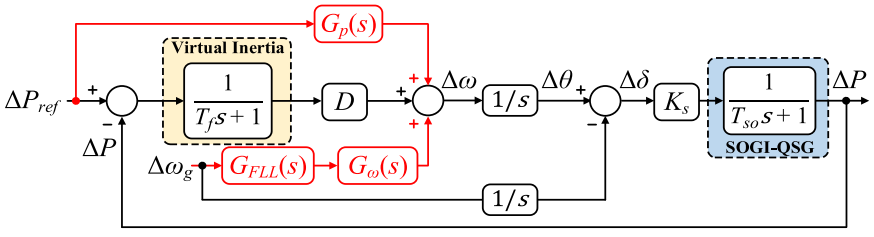

Fig. 4. Small-signal model of the proposed IAHO.

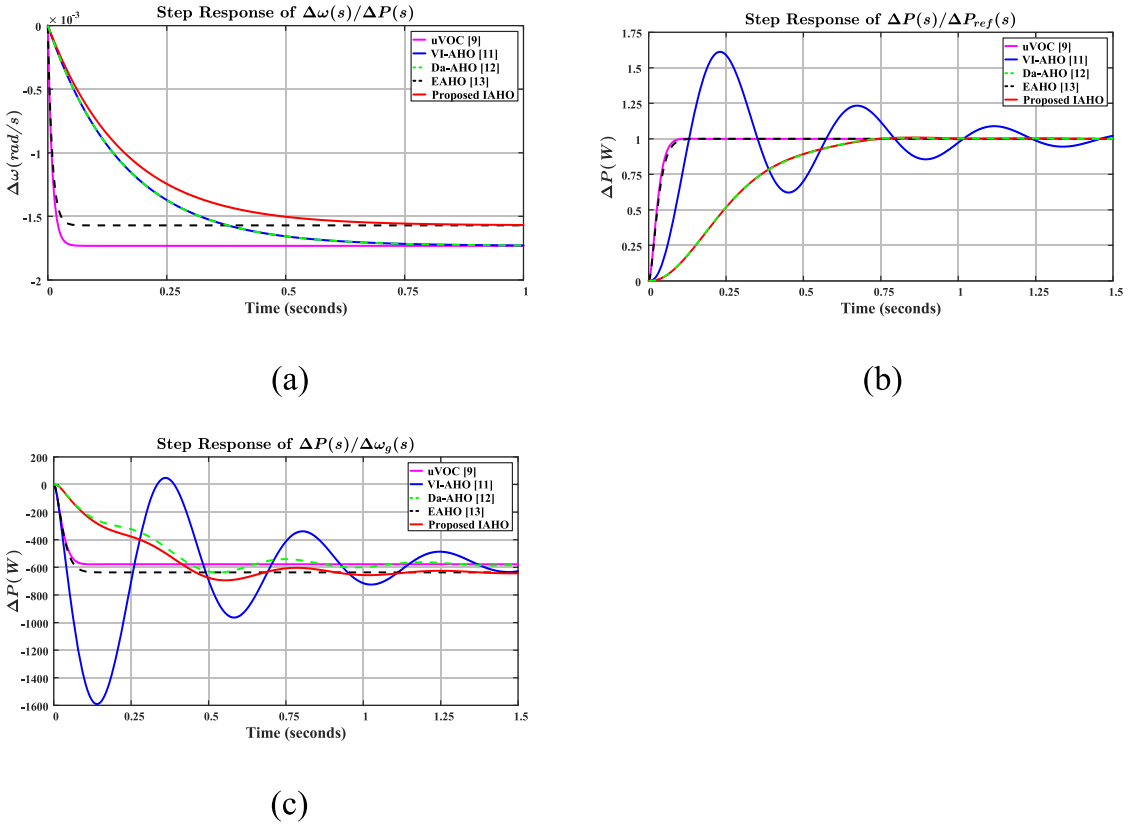

Fig. 5. Step response comparison of: (a) $\Delta\omega(s)/\Delta P(s)$, (b) $\Delta P(s)/\Delta P_{ref}(s)$, and (c) $\Delta P(s)/\Delta\omega_g(s)$.

Figs. 5(b) and 5(c) compare the active power response to step changes in the power reference and grid angular frequency, respectively. Due to the lack of virtual inertia, uVOC and EAHO exhibit first-order behaviour. VI-AHO demonstrates second-order dynamics but suffers from significant oscillatory behaviour and, therefore, large overshoot (OS) and undershoot (US). In contrast, Da-AHO and IAHO achieve well-damped responses owing to the feedforward damping enhancement. Moreover, Fig. 5(c) highlights approximately a 10 % improvement in active power support from both EAHO and IAHO compared to the other approaches. This improvement is attributed to the use of a voltage-independent APL droop coefficient, which enhances grid support during disturbances.

Fig. 6 presents the MATLAB-based step responses of $\Delta\omega(s)/\Delta P_{ref}(s)$ and $\Delta\omega(s)/\Delta\omega_g(s)$ in grid-connected mode. As shown in Fig. 6(a), the proposed IAHO and Da-AHO achieve lower frequency peaks and reduced RoCoF, indicating improved inertial performance. In contrast, uVOC and EAHO exhibit significantly higher frequency peaks and an initial large RoCoF. In addition, VI-AHO shows pronounced frequency peaks and oscillations in both responses.

3. Transient stability analysis

In general, the transient stability of an inverter depends on the dynamic response of the power angle (δ) following a large grid disturbance.

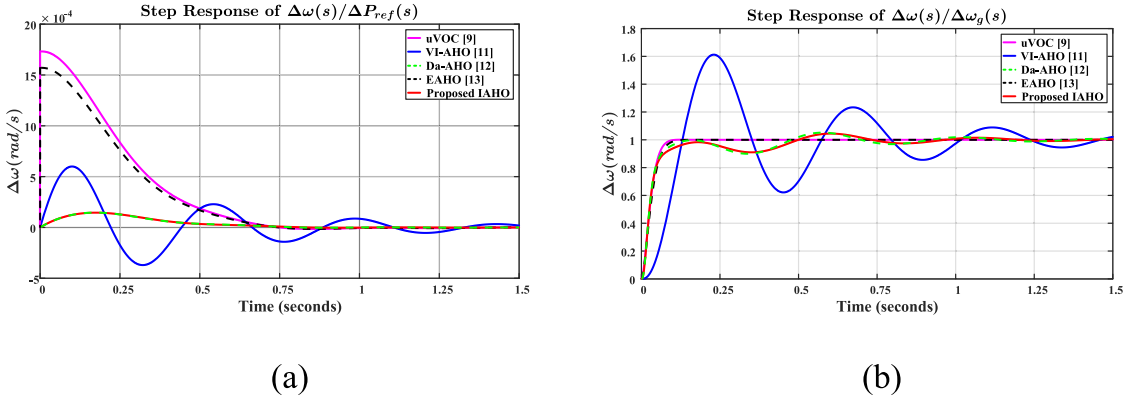

Fig. 6. Step response comparison of: (a) $\Delta\omega(s)/\Delta P_{ref}(s)$ and (b) $\Delta\omega(s)/\Delta\omega_g(s)$.

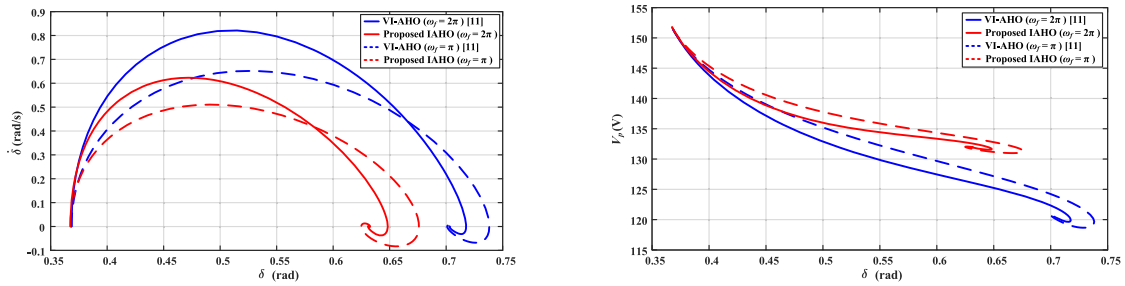

(a) (b)

Fig. 7. (a) Phase portraits and (b) V_p-δ curves when grid voltage drops to 0.7 pu.

The inverter is considered stable if δ returns to its original value or settles at a new steady state, and unstable if δ diverges.

To analyse transient stability, the simplified circuit of a GFM inverter connected to the power grid (as shown in Fig. 3) is considered. Assuming $\dot{\delta} = \omega - \omega_0$, Eq. (8) can be rewritten as:

$$\begin{cases} T_f \ddot{V}_p + \dot{V}_p = \mu\, T_f \left(V_{p0}^2 - 3V_p^2\right)\dot{V}_p + \mu \left(V_{p0}^2 - V_p^2\right)V_p + \eta V_p (Q_{ref} - Q) \\ T_f \ddot{\delta} + \dot{\nu} = \eta (P_{ref} - P) \end{cases} \tag{15}$$

where

$$\begin{cases} P = \dfrac{R_T\left(V_p^2 - V_p V_g \cos(\delta)\right) + X_T V_p V_g \sin(\delta)}{2\left(R_T^2 + X_T^2\right)} \\ Q = \dfrac{X_T\left(V_p^2 - V_p V_g \cos(\delta)\right) - R_T V_p V_g \sin(\delta)}{2\left(R_T^2 + X_T^2\right)} \end{cases}. \tag{16}$$

Since transient stability is assessed under large disturbances in grid voltage amplitude or phase, the damping improvement strategies (implemented as feedforward controllers from P_{ref} and ω_g) do not influence large-signal stability and are therefore omitted from (15). In addition, since $T_f > 15\ T_{so}$, the inertial effect associated with T_{so} is negligible and excluded for simplicity.

In the following analysis, the transient stability of the proposed IAHO is compared with conventional strategies that incorporate virtual inertia (VI-AHO and Da-AHO). Since feedforward damping is neglected in the large-signal stability analysis, both VI-AHO and Da-AHO share the same dynamic equations, given by:

$$\begin{cases} T_f \ddot{V}_p + \dot{V}_p = \mu\, T_f \left(V_{p0}^2 - 3V_p^2\right)\dot{V}_p + \mu \left(V_{p0}^2 - V_p^2\right)V_p + \dfrac{2\eta}{V_p}(Q_{ref} - Q) \\ T_f \ddot{\delta} + \dot{\delta} = \dfrac{2\eta}{V_p^2}(P_{ref} - P) \end{cases} \tag{17}$$

Because grid faults may result in high currents and laboratory experimental setups are limited in handling such conditions, the transient stability is analysed at half of the nominal voltage and current values specified in Table I and L_g=15 mH. By numerically solving the nonlinear differential equations in (15)–(17) using MATLAB, $\dot{\delta} - \delta$ and $V_p - \delta$ trajectories are obtained. Fig. 7 shows these trajectories in response to a grid voltage drop to 0.7 pu at two different virtual-inertia values, $\omega_f = 2\pi$ rad/s and $\omega_f = \pi$ rad/s. As expected, virtual inertia does not affect the steady-state operating point. The equilibrium remains (δ, V_p) = (0.63 rad, 131 V) for IAHO and (0.70 rad, 120 V) for VI-AHO, for both inertia settings. Following the fault, $\dot{\delta} > 0$, forcing δ to increase. After reaching its peak, δ decreases and settles at a new stable equilibrium point. Owing to the inertial behaviour of the controllers, the system exhibits a second-order dynamic response. However, virtual inertia clearly affects the transient behaviour. As can be seen from Fig. 7 (a), for a higher virtual inertia ($\omega_f = \pi$ rad/s), the angle δ experiences a higher OS.

Fig. 8 presents the $\dot{\delta} - \delta$ and $V_p - \delta$ trajectories when the grid voltage drops to 0.6 pu. In this case, the proposed IAHO strategy stabilises at a new equilibrium point of (0.82 rad, 123 V). In contrast, as shown in Fig. 8(a), the VI-AHO response diverges, with $\dot{\delta} > 0$ for all δ, indicating that no stable equilibrium exists in the power angle trajectory. This clearly demonstrates that the proposed strategy offers superior transient stability compared to existing virtual inertia-based approaches. This enhanced stability is primarily attributed to the improved reactive power support provided by the proposed strategy. The reactive power loop droop coefficient (m_q) of the proposed strategy can be derived from (8). In steady state, where all derivative terms vanish, $m_q = -dV_p/dQ$ to (8) leads to expressions given in (18) for both IAHO and VI-AHO:

$$\begin{cases} \text{Proposed IAHO}: \ m_q = \dfrac{\eta}{2\mu V_p} \\ \text{VI} - \text{AHO}: \ m_q = \dfrac{\eta}{\mu V_p\left(2V_p^2 - V_{p0}^2\right)} \end{cases} \tag{18}$$

Eq. (18) shows that, in the case of the VI-AHO, m_q becomes negative when $V_p < V_{p0}/\sqrt{2}$. In contrast, the proposed IAHO maintains a positive m_q for all voltage magnitudes, ensuring increased reactive power injection during voltage sags and thereby enhancing stability performance.

Fig. 9 shows the feasible region plots resulting from numerical computation. To do so, the grid voltage is fixed at 0.5 pu, and P_{ref} and Q_{ref} vary. At each (P_{ref}, Q_{ref}), the nonlinear averaged model is simulated, and the convergence of the nonlinear time-domain model to the desired equilibrium is checked. The resulting feasible-region plots, shown in Fig. 9, reveal that the proposed IAHO guarantees a substantially larger stable region than the conventional VI-AHO.

Finally, Table 2 provides a detailed comparison between the proposed IAHO and existing approaches, including uVOC [9], VI-AHO [11], Da-AHO [12], EAHO [13], and the transient-stability-oriented methods [19,20], in terms of (i) virtual inertia, (ii) damping enhancement, (iii) APL droop coefficient and its voltage dependency, and (iv) transient stability capability. As shown, IAHO is the only method that offers all of these features within a unified control framework, demonstrating its distinct advantages over existing AHO-based strategies.

4. Experimental validation

To validate the theoretical results, a single-phase 2.5 kVA, 220 V, 50 Hz H-bridge inverter, shown in Fig. 10, is implemented with the

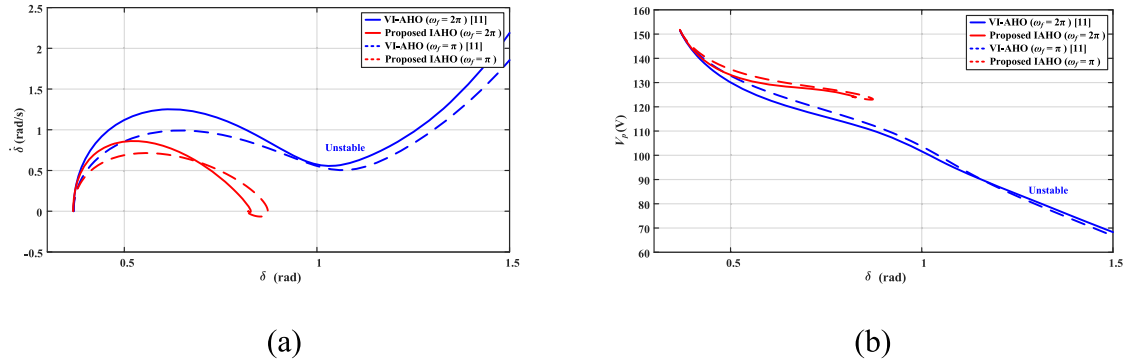

Fig. 8. (a) Phase portraits and (b) V_p-δ curves when grid voltage drops to 0.6 pu.

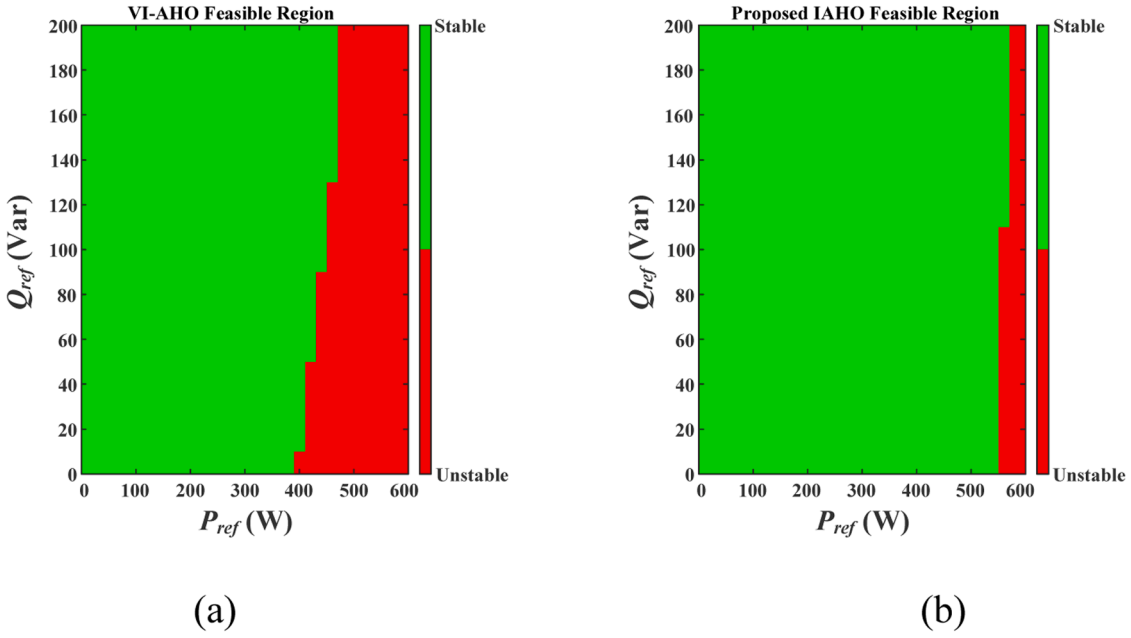

Fig. 9. Feasible P_{ref} and Q_{ref} region when grid voltage drops to 0.5 pu: (a) VI-AHO [11] and (b) proposed IAHO.

Table 2
Comparison between proposed and conventional strategies.

Strategies	Virtual inertia	Damping	APL droop coefficient (m_p) voltage-independent		Transient stability enhancement
Proposed IAHO	✓	✓	✓	($m_p = \eta$)	✓
uVOC [9]	×	×	×	($m_p = 2\eta/V_p^2$)	×
VI-AHO [11]	✓	×	×	($m_p = 2\eta/V_p^2$)	×
Da-AHO [12]	✓	✓	×	($m_p = 2\eta/V_p^2$)	×
EAHO [13]	×	×	✓	($m_p = \eta$)	✓
[19]	×	×	×	($m_p = 2\eta/V_p^2$)	✓
[20]	×	×	×	($m_p = \sqrt{2}\eta V_p$)	✓

controller highlighted in Fig. 1. A 7.5 kVA grid emulator is used to reproduce the desired grid conditions, and all control algorithms are executed on a dSPACE DS1007 real-time system. Voltage and current measurements are acquired via the DS2004 A/D board, while PWM and relay signals are generated using the DS4002 digital I/O board. A unipolar PWM strategy is adopted, with switching and sampling frequencies both set to 20 kHz ($f_{sw} = f_{sa} = 20$ kHz), as listed in Table I. The calculated active power (P) and frequency deviation ($\Delta f = f - 50$) are sent to a Tektronix MSO 5204B oscilloscope via the DS2101 D/A Board for monitoring and recording. In the experimental setup, all integrators are discretised using the third-order integrator proposed in [27]. Since the proposed strategy is built on the VOC framework and augments AHO only with low-order filters and feedback loops, its implementation burden remains comparable to existing VOC-based schemes and significantly lighter than more complex GFM approaches.

For simplicity, the DC side of the converter is implemented as a stiff voltage source, representing the short-term behaviour of a BESS [2]. In practical scenarios, however, the battery's state of charge and charging/discharging rate must be monitored, and ancillary service provision should be coordinated with charging requirements. Likewise, operation in islanded mode must comply with the allowable battery discharge limits and may need to be coordinated with residential generation sources in the islanded network. Since these functions typically operate on much slower time scales than the control loops considered in this work, they can be implemented within a higher-level hierarchical control layer for power and energy management, following frameworks

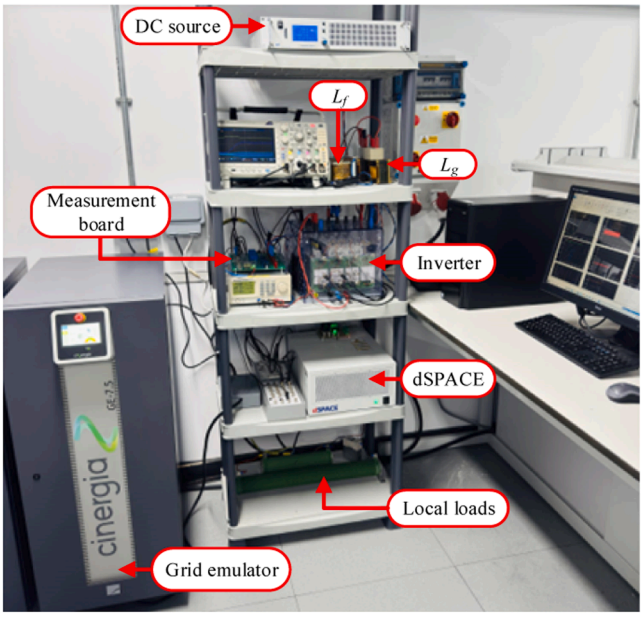

Fig. 10. Experimental test setup.

similar to [28], and are therefore not further discussed in this paper.

In the following, the effectiveness of the proposed strategy is validated in comparison to conventional ones through four test scenarios.

4.1. Test scenario 1: step change in P_{ref} in charging mode

In this scenario, all AHO-based inverters operate in grid-connected mode to evaluate their response to a step change in P_{ref}. In this paper, positive power values represent power flow from the DC source to the grid (discharging mode), while negative values correspond to charging mode. To emulate battery charging performance, P_{ref} is changed from −500 W to −2000 W.

Fig. 11 presents the results for all controllers, where Δf is the frequency deviation from its nominal value ($\Delta f = f$ - 50). As shown, all strategies successfully track the power reference. However, due to the absence of virtual inertia, uVOC in Fig. 11(a) and EAHO in Fig. 11(d) exhibit first-order active power responses, while their frequency experiences a high RoCoF and a low frequency nadir, which can jeopardise stability and trigger the system protections.

For VI-AHO (Fig. 11(b)), the frequency response achieves a lower RoCoF; nevertheless, the active power exhibits oscillatory behaviour with a high US of approximately 40 %, resulting from insufficient damping. In contrast, Da-AHO and the proposed IAHO (Figs. 11(c) and 11(e)) demonstrate well-damped responses with negligible active power US, as well as considerably smoother frequency dynamics characterised by lower RoCoF and a higher frequency nadir. These results are consistent with the theoretical predictions from the small-signal analysis, particularly those shown in Figs. 5(b) and 6(a).

4.2. Test scenario 2: step change in grid frequency

In this scenario, the active power support capability of the AHO-based inverters is evaluated under a grid frequency variation. The inverters operate with $P_{ref} = 500$ W, supplying energy from the DC source to the grid. Subsequently, the grid frequency is reduced from 50 Hz to 49.7 Hz. Since all controllers are designed with a 1 % active power droop, their output active power is expected to increase by 1200 W for a 0.3 Hz frequency drop. Fig. 12 presents the corresponding results. Similar to Test Scenario 1, all strategies exhibit well-damped responses, except for VI-AHO in Fig. 12(b), which shows oscillatory behaviour with a 70 % power OS. As shown, uVOC, VI-AHO, and Da-AHO in Figs. 12(a)–(c) deliver 1100 W active power to support the grid during the frequency variation, which is 8 % less than the expected value due to their voltage-

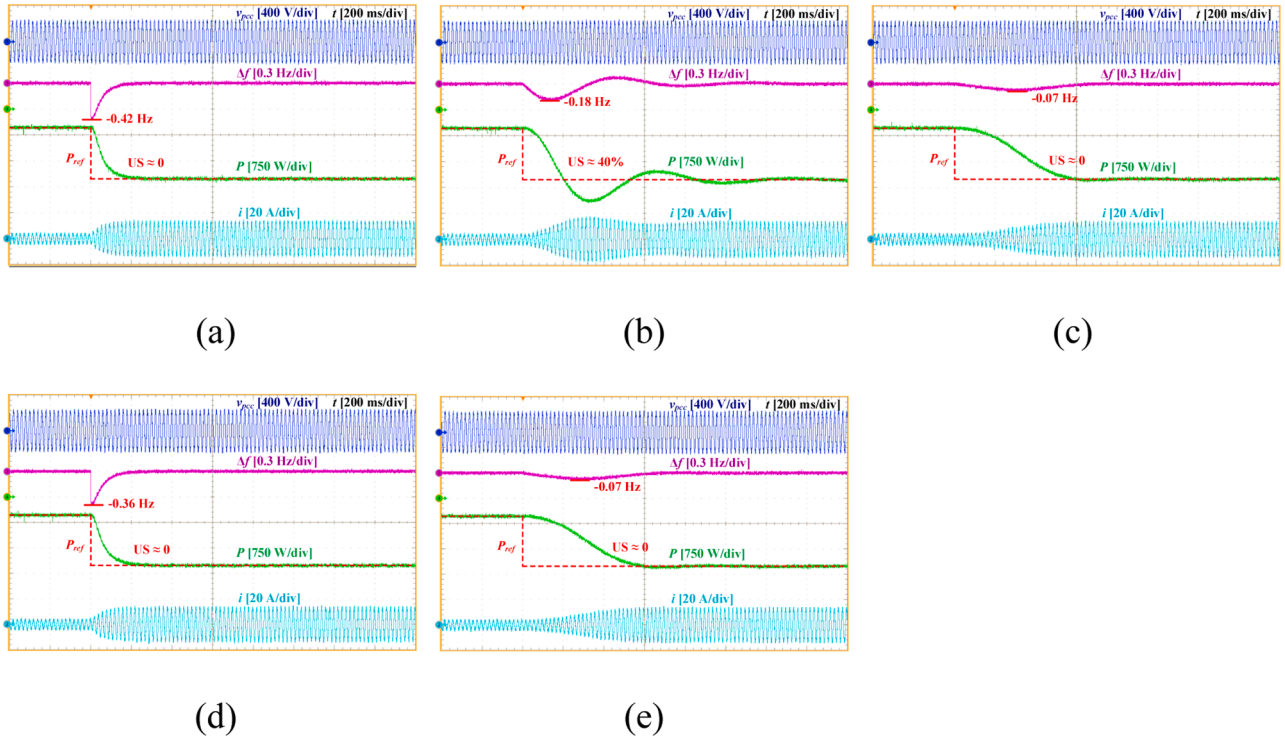

Fig. 11. Experimental results of Test Scenario 1: (a) uVOC [9], (b) VI-AHO [11], (c) Da-AHO [12], (d) EAHO [13], and (e) proposed IAHO.

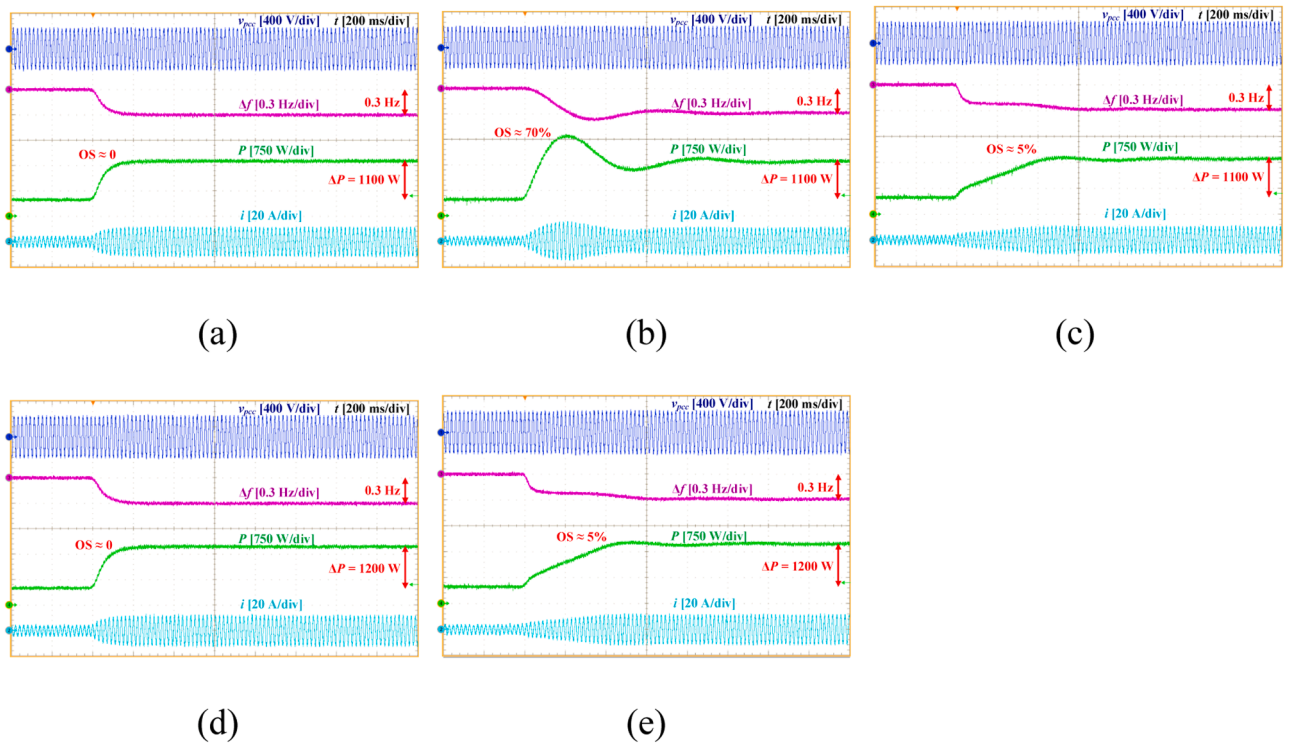

Fig. 12. Experimental results of Test Scenario 2: (a) uVOC [9], (b) VI-AHO [11], (c) Da-AHO [12], (d) EAHO [13], and (e) proposed IAHO.

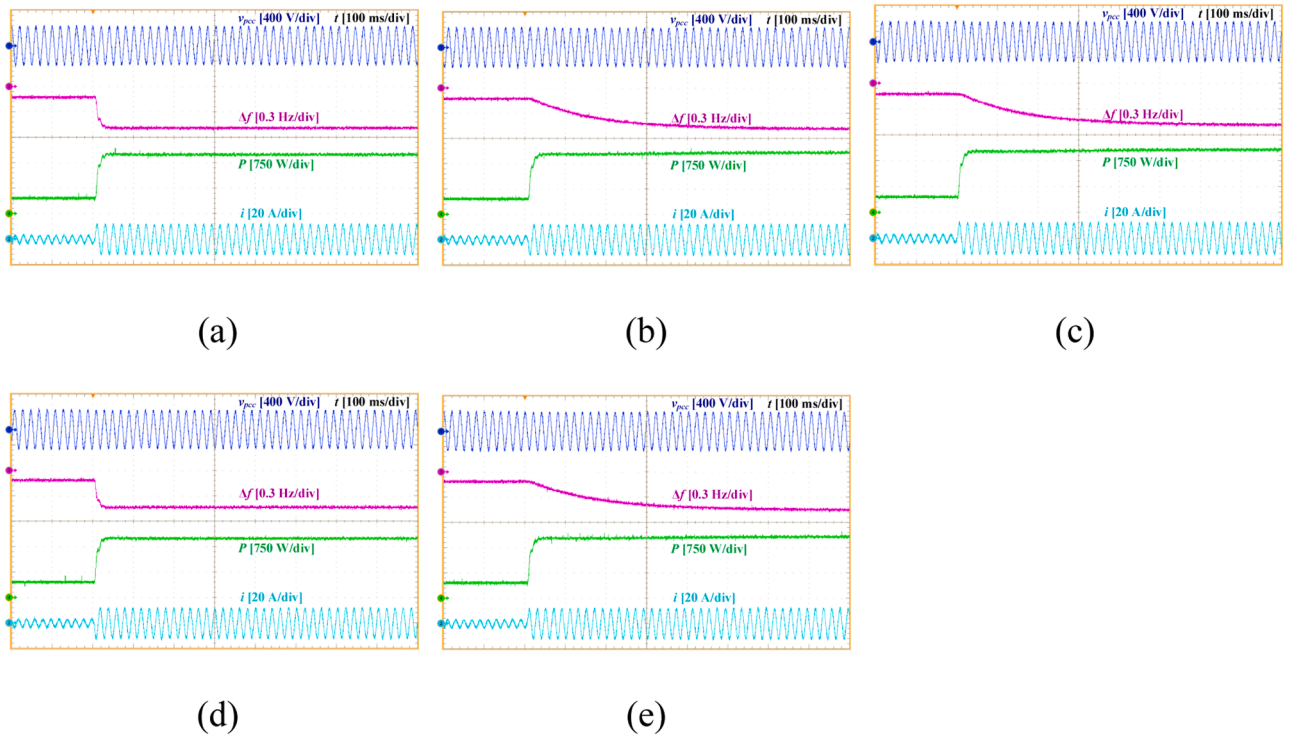

Fig. 13. Experimental results of Test Scenario 3: (a) uVOC [9], (b) VI-AHO [11], (c) Da-AHO [12], (d) EAHO [13], and (e) proposed IAHO.

dependent APL droop coefficients. By contrast, EAHO and the proposed IAHO in Figs. 12(d) and (e) achieve the full 1200 W injection, thereby providing the required support. These findings are consistent with the small-signal analysis results shown in Figs. 5(c) and 6(b).

4.3. Test scenario 3: operation in stand-alone mode

This scenario evaluates the performance of the AHO-based inverters in stand-alone mode. Initially, the inverters supply a 480 W load (100 Ω). Subsequently, an additional 33 Ω load is connected in parallel,

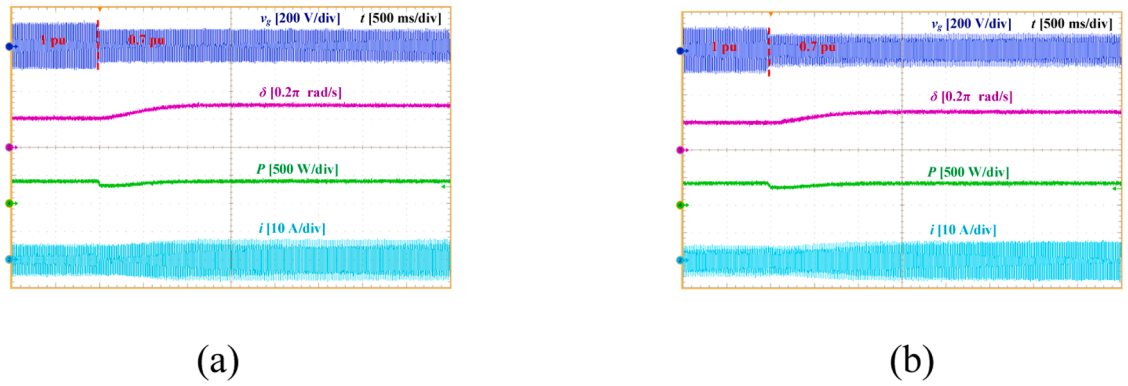

Fig. 14. Experimental results of Test Scenario 4 when grid voltage drops to 0.7 pu: (a) VI-AHO [11] and (b) proposed IAHO.

increasing the output power.

The results are shown in Fig. 13. As observed, all strategies are capable of operating in stand-alone mode, thereby providing energy during grid outages. However, due to the absence of virtual inertia in the dynamic equations of uVOC and EAHO, their frequency responses exhibit a high RoCoF, as shown in Figs. 13(a) and (d), respectively. In contrast, VI-AHO, Da-AHO, and the proposed IAHO achieve smoother frequency transitions with significantly lower RoCoF in response to local load variations, consistent with the small-signal analysis results in Fig. 5 (a).

4.4. Test scenario 4: transient stability validation

This scenario evaluates the stability performance of the proposed IAHO and VI-AHO under grid voltage sags. As outlined in Section III, the test is conducted at a nominal voltage of 110 V_{rms} with $L_g = 15$ mH.

Fig. 14 presents the results for a grid voltage drop to 0.7 pu. Before the sag, the inverters operate with $P_{ref} = 400$ W. As shown, both strategies remain stable, continuously delivering 400 W to the grid. For the proposed IAHO, the equilibrium of δ shifts from 0.62 rad/s to 0.85 rad/s before and after the voltage sag, respectively, whereas for VI-AHO, it shifts from 0.62 rad/s to 0.94 rad/s. These results are consistent with the large-signal analysis in Fig. 7, with slight deviations in the equilibrium point mainly attributed to the PWM and dead-time effects on the inverter terminal voltage.

Fig. 15 illustrates the response when the grid voltage drops to 0.6 pu. In this case, the proposed IAHO remains stable, while the VI-AHO fails to establish equilibrium points, preventing the active power from reaching its reference value. As observed in Fig. 15(a), low-frequency oscillations appear in the waveforms of P, δ, and i, indicating instability, in agreement with the results in Fig. 8.

4.5. Comparative analysis

This section compares the performance and ancillary services delivered by AHO-based strategies using the experimental results. Table 3 summarises the outcomes of Test Scenarios 1–3, where values highlighted in green indicate the best performance and those in red represent the worst.

The results demonstrate that the proposed strategy consistently outperforms conventional approaches by achieving lower RoCoF, higher frequency nadir, reduced power OS/US, and enhanced active power support during frequency variations. In summary, the proposed strategy integrates all essential ancillary services, including virtual inertia,

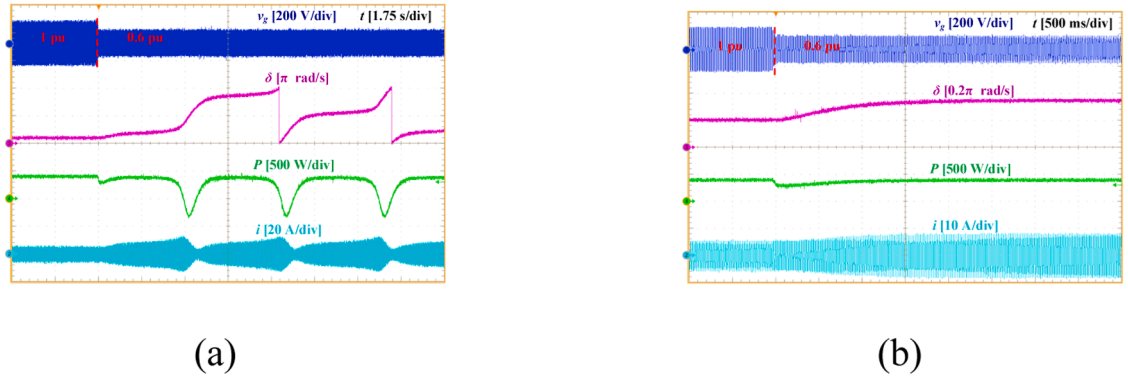

Fig. 15. Experimental results of Test Scenario 4 when grid voltage drops to 0.6 pu: (a) VI-AHO [11] and (b) proposed IAHO.

Table 3
Comparison between AHO strategies based on experimental results.

Strategies		uVOC [9]	VI-AHO [11]	Da-AHO [12]	EAHO [13]	Proposed IAHO
Test Scenario 1	RoCoF (Hz/s)	∞	1.3	0.2	∞	0.2
	Frequency nadir (Hz)	49.58	49.82	49.93	49.64	49.93
	US %	0	40	0	0	0
Test Scenario 2	P (W)	1100	1100	1100	1200	1200
	OS %	0	70	5	0	5
Test Scenario 3	RoCoF (Hz/s)	9	3.2	3.2	10	3.2

damping and improved droop performance within a unified control framework. Moreover, as confirmed in Test Scenario 4, it provides superior stability under grid voltage sags.

5. Conclusion

This paper presented an integrated AHO-based VOC strategy for single-phase GFM inverters, enabling inverter-based resources to provide ancillary services in both grid-connected and stand-alone modes. By incorporating virtual inertia, feedforward damping, and voltage-independent droop characteristics, the proposed controller addresses key limitations of existing AHO-based approaches. Analytical and experimental results confirm that the IAHO achieves smoother frequency responses with lower RoCoF, improved active power support under frequency deviations, and well-damped active power responses. Importantly, large-signal analysis and experimental tests under grid voltage sags demonstrated that the proposed method provides superior transient stability compared with other inertia-emulating strategies. Overall, the proposed IAHO offers a unified solution for virtual inertia, damping, and droop control, making it a strong candidate for BESSs to reliably support the grid, thereby facilitating the transition to a more resilient and renewable-based power system.

Funding

This research did not receive any specific grant from funding agencies in the public, commercial, or not-for-profit sectors.

CRediT authorship contribution statement

Hamed Rezazadeh: Writing – review & editing, Writing – original draft, Visualization, Validation, Methodology, Investigation, Formal analysis, Conceptualization. **Mohammad Monfared:** Writing – review & editing, Writing – original draft, Visualization, Validation, Supervision, Resources, Project administration, Methodology, Investigation, Formal analysis, Conceptualization. **Meghdad Fazeli:** Writing – review & editing, Writing – original draft, Supervision, Project administration, Methodology, Investigation, Formal analysis. **Saeed Golestan:** Writing – review & editing, Writing – original draft, Supervision, Methodology, Formal analysis, Conceptualization.

Declaration of competing interest

The authors declare that they have no known competing financial interests or personal relationships that could have appeared to influence the work reported in this paper.

This research did not receive any specific grant from funding agencies in the public, commercial, or not-for-profit sectors.

Appendix A

Fig. A1 shows the relationship between the measured current i and the input of the AHO strategy y'.

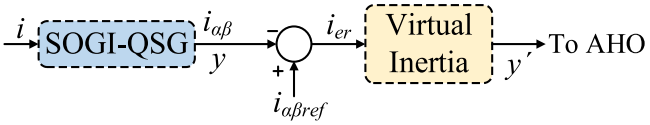

Fig. A1. Relationship between measured current and AHO's input.

The transfer function between the α-axis output of the SOGI-QSG and its input is given in (3). From this equation, its state-space representation can be written as:

$$\begin{cases} \dot{x}_1 = \omega\, x_2 \\ \dot{x}_2 = -\omega\, x_1 - K_{so}\, \omega\, x_2 + K_{so}\, \omega\, i \\ y = x_2 \end{cases} \tag{A1}$$

where $x_1 = X \sin(\gamma)$, $x_2 = X \cos(\gamma)$, and $i = I \cos(\gamma)$. By defining $X = \sqrt{x_1^2 + x_2^2}$, its time derivative is:

$$\dot{X} = \frac{x_1 \dot{x}_1 + x_2 \dot{x}_2}{X} = -K_{so}\omega X \cos^2(\gamma) + K_{so}\omega I \cos^2(\gamma) \tag{A2}$$

Averaging over one AC cycle and considering $Y = X$ from A1, one can write:

$$\frac{\overline{Y}(s)}{\overline{I}(s)} = \frac{K_{so}\omega/2}{s + K_{so}\omega/2} = \frac{1}{T_{so}\, s + 1} \tag{A3}$$

where the bar denotes the fundamental-frequency (cycle-averaged) component. For the virtual inertial block (resonant controller), following an identical averaging approach one can write:

$$\frac{\overline{Y'}(s)}{\overline{I_{er}}(s)} = \frac{\omega_f}{s + \omega_f} = \frac{1}{T_f\, s + 1}. \tag{A4}$$

where $\overline{I_{er}} = I_{ref} - \overline{Y}$. From Fig. 1, the control law of AHO was obtained in (1). By defining $v_\alpha = V_p \cos(\theta)$, $v_\beta = V_p \sin(\theta)$, $y_\alpha = Y\cos(\theta+\varphi)$, $y_\beta = Y\sin(\theta+\varphi)$, and $y'_\alpha = Y\cos(\theta+\varphi)$, and $y'_\beta = Y\sin(\theta+\varphi)$, Eq. (1) can be rewritten as (A5), where φ is the phase difference between the inverter's voltage and current.

$$\begin{cases} \dot{v}_\alpha = \mu\left(V_{p0}^2 - V_p^2\right)v_\alpha - \omega_0^{'}v_\beta - \dfrac{\eta V_p^2}{2}y'_\beta \\ \dot{v}_\beta = \omega_0^{'}v_\alpha + \mu\left(V_{p0}^2 - V_p^2\right)v_\beta + \dfrac{\eta V_p^2}{2}y'_\alpha \end{cases} \tag{A5}$$

With θ=arctan(v_β/v_α) and $V_p = \sqrt{v_\alpha^2 + v_\beta^2}$ their time derivatives can be expressed as:

$$\begin{cases} \dot{\theta} = \dfrac{\dot{v}_\beta\, v_\alpha - \dot{v}_\alpha v_\beta}{V_p^2} \\ \dot{V}_p = \dfrac{v_\alpha \dot{v}_\alpha + v_\beta\, \dot{v}_\beta}{V_p} \end{cases} \tag{A6}$$

Substituting (A5) into (A6) results in:

$$\begin{cases} \dot{\theta} = \omega_0^{'} + \dfrac{\eta V_p Y'}{2}(\cos(\theta+\varphi)\cos(\theta) + \sin(\theta+\varphi)\sin(\theta)) \\ \dot{V}_p = \mu\left(V_{p0}^2 - V_p^2\right)V_p + \dfrac{\eta V_p^2 Y'}{2}(\cos(\theta+\varphi)\sin(\theta) - \sin(\theta+\varphi)\cos(\theta)) \end{cases} \tag{A7}$$

Averaging over one AC cycle and substituting $\overline{Y'}$ and $\overline{Y}$ from (A4) and (A3) results in (8), where $P = 0.5\ \overline{V_p}\ \bar{I}\cos(\varphi)$, $Q = 0.5\ \overline{V_p}\ \bar{I}\sin(\varphi)$, P_{ref}=$0.5\ \overline{V_p}\ I_{ref}\cos(\varphi)$, and Q_{ref}=$0.5\ \overline{V_p}\ I_{ref}\sin(\varphi)$.

Data availability

Data will be made available on request.

References

[1] H. Rezazadeh, M. Monfared, M. Fazeli, S. Golestan, Single-phase grid-forming inverters: a review, in: *2023 International Conference on Computing, Electronics & Communications Engineering (iCCECE)*, IEEE, 2023, pp. 7–10, https://doi.org/10.1109/iCCECE59400.2023.10238661. Aug.

[2] J.A. Suul, S. DArco, G. Guidi, Virtual synchronous machine-based control of a single-phase Bi-directional battery charger for providing vehicle-to-grid services, IEEE Trans. Ind. Appl. 52 (4) (2016) 3234–3244, https://doi.org/10.1109/TIA.2016.2550588. Jul.

[3] T. Shao, T.Q. Zheng, H. Li, X. Zhang, Parameter design and hot seamless transfer of single-phase synchronverter, Electr. Power Syst. Res. 160 (2018) 63–70, https://doi.org/10.1016/j.epsr.2018.02.006. Jul.

[4] D. Raisz, T.T. Thai, A. Monti, Power control of virtual oscillator controlled inverters in grid-connected mode, IEEE Trans. Power Electron. 34 (6) (2019) 5916–5926, https://doi.org/10.1109/TPEL.2018.2868996.

[5] B.B. Johnson, S.V. Dhople, A.O. Hamadeh, P.T. Krein, Synchronization of parallel single-phase inverters with virtual oscillator control, IEEE Trans. Power Electron. 29 (11) (2014) 6124–6138, https://doi.org/10.1109/TPEL.2013.2296292.

[6] B.B. Johnson, M. Sinha, N.G. Ainsworth, F. Dorfler, S.V. Dhople, Synthesizing virtual oscillators to control islanded inverters, IEEE Trans. Power Electron. 31 (8) (2016) 6002–6015, https://doi.org/10.1109/TPEL.2015.2497217. Aug.

[7] M. Lu, S. Dutta, V. Purba, S. Dhople, B. Johnson, A grid-compatible virtual oscillator controller: analysis and design, in: *2019 IEEE Energy Conversion Congress and Exposition (ECCE)*, IEEE, 2019, pp. 2643–2649, https://doi.org/10.1109/ECCE.2019.8913128. Sep.

[8] M. Lu, Virtual oscillator grid-forming inverters: state of the art, modeling, and stability, IEEE Trans. Power Electron. 37 (10) (2022) 11579–11591, https://doi.org/10.1109/TPEL.2022.3163377. Oct.

[9] M.A. Awal, I. Husain, Unified virtual oscillator control for grid-forming and grid-following converters, IEEE J. Emerg. Sel. Top. Power Electron. 9 (4) (2021) 4573–4586, https://doi.org/10.1109/JESTPE.2020.3025748. Aug.

[10] H. Rezazadeh, M. Monfared, M. Fazeli, S. Golestan, Providing inertial response with unified VOC for single-phase GFM inverters, in: *2024 International Symposium on Electrical, Electronics and Information Engineering (ISEEIE)*, IEEE, 2024, pp. 94–98, https://doi.org/10.1109/ISEEIE62461.2024.00025. Aug.

[11] S. Luo, W. Chen, X. Li, Z. Hao, A new virtual inertial strategy for Andronov–Hopf oscillator based grid-forming inverters, IEEE J. Emerg. Sel. Top. Power Electron. 12 (2) (2024) 1995–2005, https://doi.org/10.1109/JESTPE.2024.3370171. Apr.

[12] H. Rezazadeh, M. Monfared, M. Fazeli, S. Golestan, Enhancing damping in single-phase grid-forming virtual oscillator control inverters: a feedforward strategy, IEEE Open J. Ind. Electron. Soc. 6 (2025) 1101–1115, https://doi.org/10.1109/OJIES.2025.3588677. July.

[13] H. Rezazadeh, M. Monfared, M. Fazeli, and S. Golestan, "Voltage-independent active-power droop coefficient for enhanced Andronov-hopf oscillator grid-forming inverters," Nov. 2025, doi: 10.48550/arXiv.2511.05252.

[14] H. Rezazadeh , M. Monfared , M. Fazeli , S. Golestan , Virtual oscillator control for grid-forming inverters: an overview of recent developments and small-signal analysis , in: 2025 Energy Conversion Congress & Expo Europe (ECCE Europe) , IEEE , United Kingdom, 2025, pp. 1 –6, https://doi.org/10.1109/ECCE-Europe62795.2025.11238644.

[15] H. Rezazadeh, M. Monfared, M. Fazeli, S. Golestan, Virtual oscillator control for grid-forming inverters: recent advances, comparative evaluation, and small-signal analysis, Energies 18 (22) (2025) 5981, https://doi.org/10.3390/en18225981.

[16] D. Pan, X. Wang, F. Liu, R. Shi, Transient stability of voltage-source converters with grid-forming control: a design-oriented study, IEEE J. Emerg. Sel. Top. Power Electron. 8 (2) (2020) 1019–1033, https://doi.org/10.1109/JESTPE.2019.2946310. Jun.

[17] H. Yu, M.A. Awal, H. Tu, I. Husain, S. Lukic, Comparative transient stability assessment of droop and dispatchable virtual oscillator controlled grid-connected inverters, IEEE Trans. Power Electron. 36 (2) (2021) 2119–2130, https://doi.org/10.1109/TPEL.2020.3007628. Feb.

[18] M. Al Talaq, M.B. Abdelghany, A. Al-Durra, H. Zeineldin, T. EL-Fouly, A sophisticated grid-forming dispatchable-virtual oscillator control with robust inner current control for improving transient stability, IEEE Trans. Power Electron. 40 (10) (2025) 15064–15079, https://doi.org/10.1109/TPEL.2025.3575573. Oct.

[19] S. Luo, W. Chen, Z. Hao, Y. Wang, A transient stability enhanced Andronov-hopf oscillator for grid-forming converters, IEEE Trans. Power Electron. 39 (9) (2024) 10853–10864, https://doi.org/10.1109/TPEL.2024.3404426. Sep.

[20] L. Li, et al., Transient stability analysis and enhanced control strategy for Andronov-Hopf oscillator based inverters, IEEE Trans. Energy Convers. 40 (2) (2025) 995–1008, https://doi.org/10.1109/TEC.2024.3505899. Jun.

[21] X. Xiong, X. Li, B. Luo, M. Huang, C. Zhao, F. Blaabjerg, An additional damping torque method for low-frequency stability enhancement of virtual synchronous generators, IEEE Trans. Power Electron. 39 (12) (2024) 15858–15869, https://doi.org/10.1109/TPEL.2024.3445349. Dec.

[22] C. Li, et al., Generalized stabilizer-oriented design for GFVSG integrated into weak-stiffness power networks, IEEE Trans. Power Syst. 37 (6) (2022) 4958–4961, https://doi.org/10.1109/TPWRS.2022.3193032. Nov.

[23] X. Xiong, C. Wu, B. Hu, D. Pan, F. Blaabjerg, Transient damping method for improving the synchronization stability of virtual synchronous generators, IEEE Trans. Power Electron. 36 (7) (2021) 7820–7831, https://doi.org/10.1109/TPEL.2020.3046462. Jul.

[24] C. Li, Y. Yang, F. Blaabjerg, Mechanism analysis for oscillation transferring in grid-forming virtual synchronous generator connected to power network, IEEE Trans. Ind. Electron. 72 (8) (2025) 8715–8720, https://doi.org/10.1109/TIE.2025.3531473. Aug.

[25] S. Golestan, J.M. Guerrero, J.C. Vasquez, A.M. Abusorrah, Y. Al-Turki, Standard SOGI-FLL and its close variants: precise modeling in LTP framework and determining stability region/robustness metrics, IEEE Trans. Power Electron. 36 (1) (2021) 409–422, https://doi.org/10.1109/TPEL.2020.2997603. Jan.

[26] Task Force C6.04.02, *Benchmark Systems for Network Integration of Renewable and Distributed Energy Resources*, CIGRE Brochure No. 575, Paris, France, ISBN: 978-2-85873-270-8, 2014.

[27] M. Ciobotaru, R. Teodorescu, F. Blaabjerg, A new single-phase PLL structure based on second order generalized integrator, in: *2006 37th IEEE Power Electronics Specialists Conference*, IEEE, 2006, pp. 1–6, https://doi.org/10.1109/pesc.2006.1711988. Jun.

[28] J.M. Guerrero, J.C. Vasquez, J. Matas, L.G. de Vicuna, M. Castilla, Hierarchical control of droop-controlled AC and DC microgrids—a general approach toward standardization, IEEE Trans. Ind. Electron. 58 (1) (2011) 158–172, https://doi.org/10.1109/TIE.2010.2066534. Jan.